

Surface Alignment of an Elastic Body Using a Multiresolution Wavelet Representation

Smadar Gefen, *Member, IEEE*, Oleh Tretiak*, *Senior Member, IEEE*, Louise Bertrand, Glenn D. Rosen, and Jonathan Nissanov, *Member, IEEE*

Abstract—An algorithm for nonlinear registration of an elastic body is developed. Surfaces (outlines) of known anatomic structures are used to align all other (internal) points. The deformation field is represented with a multiresolution wavelet expansion and is modeled by the partial differential equations of linear elasticity. A hierarchical approach that reduces algorithm complexity is adopted. The performance of the algorithm is evaluated by two-dimensional alignment of sections from mouse brains located in the olfactory bulbs. The registration algorithm was guided by manually delineated contours of a subset of brain structures and validated based on another subset of brain structures. The wavelet alignment algorithm produced a twofold to fivefold improvement in accuracy over an affine (linear) alignment algorithm.

Index Terms—Elastic deformation, nonlinear registration, segmentation, wavelet.

I. INTRODUCTION

IMAGE registration is a widely required task in multidimensional data visualization and analysis. In medicine, image alignment is used to fuse complementary information (across subjects and modalities as well as within) and to construct a probabilistic map. Image registration as a general solution in computer vision and in biomedicine in particular has been widely explored [1]–[3]. Four main characteristics distinguish one registration algorithm from another: 1) the features that drive the registrations—these can be image-based or geometric; 2) the transformation model, whether it is linear or nonlinear; 3) the similarity measures based on which the alignment accuracy is determined; and 4) the optimization method with which the transformation parameters are estimated. Survey papers dealing with the classification of registration methods can be found in the literature (see [4]–[7]).

A common biomedical problem where image registration has been employed is in mapping newly acquired experimental datasets (called the *test brains*) onto a canonical atlas (called the *reference brain*). By doing so, one can segment these sets

using standard neuro-anatomical templates. Registration of biomedical images, for this purpose and in general whenever intersubject alignment is contemplated, is complicated by the inevitable presence of geometric variability. This necessitates the use of nonlinear transformation if significant accuracy is desired. In addition, corresponding features used to guide registration are difficult to identify.

A number of approaches have been adopted to compensate for nonlinear differences between objects to be aligned including modeling one object as an elastic deformed version of the other. Among these are many that relied on Duchon's [8] and Meinguet's [9] introduction of the thin-plate splines as a mathematical interpolator. Goshtasby [10] and Bookstein [11] applied this interpolator to two-dimensional (2-D) image registration. Gabrani and Tretiak [12], [13] extended Bookstein's method to three-dimensional (3-D) image registration. In the thin-plate splines method, the image is modeled as a metal plate in which landmark points are deformed in the x and y directions separately. Coefficients of radial basis functions that interpolate the deformation are computed such that an elastic energy functional is minimized.

Another approach to nonlinear registration uses the Navier linear partial differential equation (PDE) to model an elastic object's deformation. The Navier PDE modeling of organ tissues as an elastic object, adopted from continuum mechanics, considers the organs to be elastic mediums that are exposed to external forces and are smoothly deformed. Bajcsy and Broit [14], [15] were the first to apply Navier PDE to registration. In their method, an equilibrium state between external and internal forces was reached for an isotropic homogeneous body. The external forces were determined in such a way that an image-based similarity metric is maximized. Similarly, Davatzikos [16] used a deformable surface parametric representation of the brain's external surface to map one brain surface onto another based on extracted surface (geometric) features. The elastic mapping of one brain volume to another was found by solving the differential equation that models an inhomogeneous elastic body under external forces. The external forces were determined so that the known cortical mapping was satisfied.

In the nonlinear registration case, where many registration parameters are involved, misregistration might occur due to the difficulty in finding a global minimum in the presence of many local minima. The coarse-to-fine strategy in the optimization process can prevent convergence into local minima traps. For example, Thevenaz *et al.* [17] proposed an image-based linear registration algorithm; an image pyramid was built using cubic B-spline interpolator and a coarse-to-fine iterative strategy was

Manuscript received November 1, 2002; revised September 23, 2003. This work was supported by the National Institutes of Health (NIH) under Award P20 MH62009. Asterisk indicates corresponding author.

S. Gefen, L. Bertrand, and J. Nissanov are with the Computer Vision Laboratory for Vertebrate Brain Mapping, Department of Neurobiology and Anatomy, Drexel College of Medicine, Drexel University, Philadelphia, PA 19129-1096 USA.

*O. Tretiak is with the Electrical and Computer Engineering Department, Drexel University, Philadelphia, PA 19104 USA (e-mail: tretiak@ece.drexel.edu).

G. D. Rosen is with the Department of Neurology, Beth Israel Deaconess Medical Center, Harvard University, Boston, MA 02215 USA.

Digital Object Identifier 10.1109/TBME.2004.827258

taken to estimate the affine transformation that minimize an intensity difference between a reference and a test data set. Lester [7] classified nonlinear hierarchical registration methods based on a gradual increase in data complexity, warp complexity, and model complexity. An alternative representation of the elastic deformation signal is wavelet multiresolution representation. The wavelet, being an inherently hierarchical representation of a signal, is naturally suitable for such progressive (coarse-to-fine) optimization starting from the low-resolution approximation of the signal (global deformation), through the details in its different orientations, and ending with the finest details of the signal (local deformation).

In this study, we have used wavelets to represent the deformation which was modeled as a combination of components that range between global deformations (best represented by the lower resolution levels of the wavelet decomposition) and local deformations (best represented by the higher resolution levels of the wavelet decomposition). The wavelet coefficients that correspond to each different signal component were estimated separately and progressively, starting from global deformation down to local deformation. This progressive approach for recovering the deformation signal is effective for reducing algorithm complexity. The elastic deformation of each signal component was estimated by minimizing the elastic energy (which is equivalent to solving for the static homogenous Navier PDE) as well as by minimizing the sum of squared distances between corresponding surfaces (which is equivalent to imposing boundary conditions).

The wavelet-based registration method presented here is characterized as follows: 1) the algorithm is driven by geometrical features with the brain's external and internal surfaces used to guide the registration algorithm; 2) the transformation model is a nonlinear deformation field where the region within the brain's volume is modeled by a wavelet multiresolution representation; 3) the similarity metric used is based on the sum of squared distances where a distance is the interval between a point on the test surface and the closest point to it on the reference surface; and 4) a progressive version of the Marquardt–Levenberg (M-L) optimization algorithm is used to minimize a functional that is the sum of two terms, namely the sum of squared distances and the elastic energy. While the alignment algorithm formulated here is a 2-D version, its generalization into a 3-D one is straightforward. The performance of the algorithm was demonstrated for the 2-D case of mouse brain mapping, focusing on the olfactory bulbs, a brain area where sensory information from the nose is processed. In our experiments, manually delineated contours of a subset of brain structures were used by the registration algorithm and another subset of brain structures were used for validation.

Wavelets have been used by several researchers for the application of image registration, either in order to represent the nonlinear deformation between two images [18], [19] or to represent the intensities of images' pixels [20]. Amit [18] used wavelet basis as well as Fourier basis to represent the deformation. He used a gradient descent optimization method to minimize the mean of squared distances between intensities of corresponding pixels. Similarly, Downie [19] used a simulated annealing op-

timization method to find the wavelet coefficients that minimize the sum of squared distances between intensities of corresponding pixels. Both algorithms, given in [18] and [19], are image-based and as such most suited for applications dealing with intramodality scans. In contrast, the registration algorithm, developed in this study, is based on geometric features; alignment is guided by objects' contours and surfaces and therefore can be used for applications dealing with intermodality as well as intramodality scans.

The remainder of the paper is organized as follows. Section II presents the wavelet representation of the elastic deformation. Next, in Section III, the registration algorithm is described. An algorithm evaluation with synthetic data is presented in Section IV. Section V evaluates the application of registration for the anatomical localization of internal structures within the olfactory bulbs of mouse brains. Section VI concludes with a discussion and suggestions for future research.

II. WAVELET REPRESENTATION OF THE ELASTIC DEFORMATION

In a registration algorithm, the objective is to find the registration parameters that result in the best geometric correspondence between the *test object* and the *reference object*. Let us define an elastic deformation field $\mathbf{u}(\mathbf{x})$ that is represented by an orthogonal wavelet decomposition. In a registration procedure, we look for the wavelet parameter vector, \mathbf{c} , that yields

$$\begin{aligned} x' &= x + u^1(x, y; \mathbf{c}) \\ y' &= y + u^2(x, y; \mathbf{c}) \end{aligned}$$

where (x, y) are coordinates in the test object space and (x', y') are corresponding coordinates in the reference object space. The registration algorithm estimates \mathbf{c} by minimizing: 1) the sum of squared Euclidian distances between points on the test object's contours and points on the corresponding reference object's contours and 2) the elastic energy of the deformation. Details are provided in Section III.

As mentioned above, the elastic deformation is represented by a wavelet multiresolution approximation. The theory of multiresolution analysis (MRA) can be found in many sources (see [21]–[23], for example). The 2-D separable wavelet decomposition of a deformation signal, $\mathbf{u}(\mathbf{x})$, everywhere within a rectangular support $\mathbf{N} = (N_x, N_y)$ is given by

$$\begin{aligned} u(\mathbf{x})^i &= \sum_{\mathbf{k}=0}^{N_j-1} 2^{-j} c_{j\mathbf{k}}^{i1} \Phi^1(2^{-j}\mathbf{x} - \mathbf{k}) \\ &+ \sum_{j=R}^J 2^{-j} \sum_{s=2}^4 \sum_{\mathbf{k}=0}^{N_j-1} c_{j\mathbf{k}}^{is} \Phi^s(2^{-j}\mathbf{x} - \mathbf{k}) \quad (1) \end{aligned}$$

where i is an index denoting the two directions x and y of the vector function $\mathbf{u}(\mathbf{x})$, s is an index denoting the subband (quadrant/orientation), j is an index denoting the resolution levels, and $\mathbf{k} = (k_x, k_y)$ is the translational index within the $N_j \equiv 2^{-j}\mathbf{N} = 2^{-j}(N_x, N_y)$ support. Each wavelet coefficient $c_{j\mathbf{k}}^{is}$ is indexed by the direction (i), the orientation (s), the resolution (j), and the spatial location (\mathbf{k}) it stands for. The basis functions

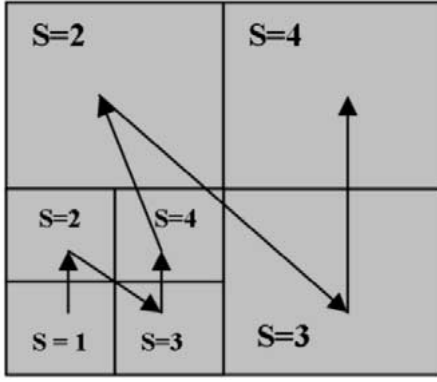


Fig. 1. Progressive order in which registration parameters were estimated.

$\Phi_{jk}^s \equiv \Phi^s(2^{-j}\mathbf{x} - \mathbf{k})$ are a tensor product of the one-dimensional (1-D) *scaling* and *wavelet* functions as follows:

$$\begin{aligned}\Phi^1 &= \phi(2^{-j}x - k_x)\phi(2^{-j}y - k_y) \\ \Phi^2 &= \phi(2^{-j}x - k_x)\psi(2^{-j}y - k_y) \\ \Phi^3 &= \psi(2^{-j}x - k_x)\phi(2^{-j}y - k_y) \\ \Phi^4 &= \psi(2^{-j}x - k_x)\psi(2^{-j}y - k_y).\end{aligned}\quad (2)$$

In this study, we have looked at three compactly supported orthogonal wavelets: Coiflets of order 3 (Coif3), Daubechies of order 5 (Db5), and Symlets of order 5 (Sym5). These wavelets have the highest number of vanishing moments for a given support, a property that affect their approximation accuracy [24]. The Coif3, Db5, and Sym5 are smooth wavelets with a support of 17, 9, and 9, respectively. Consequently, these wavelets are suitable to represent the supposedly smooth deformation signal.

Note that, if $\mathbf{u}(\mathbf{x}) \in V_{R-1}$ where V_{R-1} is a linear subspace, then (1) is a perfect representation of $\mathbf{u}(\mathbf{x})$. Since we only assume that the elastic deformation is in L^2 , (1) is merely an approximation to $\mathbf{u}(\mathbf{x})$. The accuracy of this approximation controlled by our choice of the index R that ranges here between 1 and J , where $2^{J+1} = \min(N_x, N_y)$. Consequently, for example, in the case where $N_x = N_y$, the number of parameters N_c required to define a deformation in one direction is $N_c \equiv 4 \cdot 2^{2(J-R+1)}$.

In our proposed algorithm, we split the wavelet coefficients into groups classified by the subband and the level of resolution they represent in order to reduce the number of parameters the optimization algorithm deals with at a time. Each such group of wavelet coefficients corresponds to a different component of the deformation. In other words, the deformation is a combination of components with different levels of details (resolution levels) and orientations (subbands). A progressive approach is applied in which the wavelet coefficients that correspond to a low-resolution signal component are estimated first and the wavelet coefficients that correspond to a high-resolution signal component are estimated last. Fig. 1 shows the order in which the wavelet coefficients are optimized.

III. ALGORITHM DESCRIPTION

The registration of one elastic object to its homologue is done by estimating the nonlinear deformation that brings together

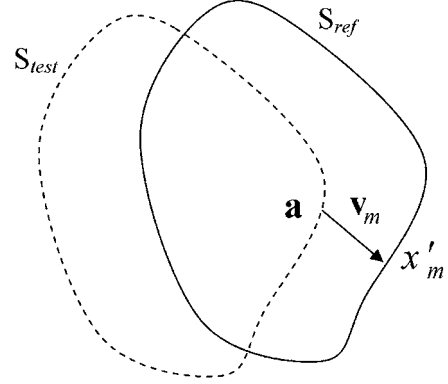


Fig. 2. Contour distance $d_m = \|\mathbf{v}_m\| = \|\mathbf{a} - \mathbf{x}'_m\|$, where \mathbf{a} is a point on the test contour ($\mathbf{a} \in S_{\text{test}}$), and \mathbf{x}'_m is the closest point to it along the reference contour ($\mathbf{x}'_m \in S_{\text{ref}}$).

a pair of corresponding contours (and, in the 3-D case, corresponding surfaces). The deformation is determined by the registration parameters—the wavelet coefficients c_{jk}^{is} —that minimize the functional $E(\mathbf{c})$. We define a functional $E(\mathbf{c})$ as the weighted sum of the sum of squared contour distances, $e(\mathbf{c})$, and the elastic energy, $L(\mathbf{c})$, so that $E(\mathbf{c}) = e(\mathbf{c}) + \omega \cdot L(\mathbf{c})$. The parameter ω is a weight constant that is empirically determined. Sections III-A and III-B below present the derivations of $e(\mathbf{c})$ and $L(\mathbf{c})$ as a function of the registration parameters, respectively. Section III-C describes in detail the M-L-based optimization procedure applied in the proposed wavelet-based registration algorithm.

A. $e(\mathbf{c})$ —Sum of Squared Contour Distances

We define $e(\mathbf{c})$ as the sum of squared contour distances where contour distance is defined as the distance between corresponding points on the test and reference contours. Since in practice the corresponding points are unknown, an estimation for this distance, $d_m \equiv \|\mathbf{a}(\mathbf{x}_m, \mathbf{c}) - \mathbf{x}'_m\|$, is used. Hence, the contour distance d_m is the Euclidean distance between an already mapped point from the test contour, $\mathbf{a}(\mathbf{x}_m \in S_{\text{test}}, \mathbf{c})$ and the closest point to it on the reference contour, $\mathbf{x}'_m \in S_{\text{ref}}$ (see Fig. 2). Similarly, a vector distance is defined as $\mathbf{v}_m \equiv \mathbf{a} - \mathbf{x}'_m$. Note that $d_m = \|\mathbf{v}_m\|$. Therefore, the magnitude being minimized is

$$e(\mathbf{c}) = \sum_{m=1}^M d_m^2 \cong \sum_{m=1}^M d(\mathbf{a}(\mathbf{x}_m, \mathbf{c}), \mathbf{x}'_m)^2. \quad (3)$$

Local dependency of $e(\mathbf{c})$ on the registration parameters \mathbf{c} is achieved by substituting the Taylor expansion of d_m in the vicinity of \mathbf{c}_1 as follows:

$$\begin{aligned}e(\mathbf{c}) &\approx \sum_{m=1}^M [d_m(\mathbf{c}_1) + \Delta^T \text{grad}_{\mathbf{c}} d_m(\mathbf{c}_1)]^2 \\ &= \sum_{m=1}^M [d_m^2(\mathbf{c}_1) + 2d_m(\mathbf{c}_1)\Delta^T \text{grad}_{\mathbf{c}} d_m(\mathbf{c}_1) \\ &\quad + \Delta^T \text{grad}_{\mathbf{c}} d_m(\mathbf{c}_1)\text{grad}_{\mathbf{c}} d_m(\mathbf{c}_1)^T \Delta] \\ &= e(\mathbf{c}_1) + \Delta^T \mathbf{b} + \Delta^T \mathbf{A} \Delta\end{aligned}\quad (4)$$

where

$$\mathbf{b}_p \equiv 2 \sum_{m=1}^M d_m(\mathbf{c}_l) \frac{\partial d_m(\mathbf{c}_l)}{\partial c_p}$$

$$A_{pq} \equiv \sum_{m=1}^M \frac{\partial d_m(\mathbf{c}_l)}{\partial c_p} \frac{\partial d_m(\mathbf{c}_l)}{\partial c_q}$$

and

$$\Delta \equiv (\mathbf{c} - \mathbf{c}_l).$$

Next, the term $\partial d_m(\mathbf{c}_l)/\partial c$ in (4) is calculated. The Euclidean distance d_m has the property that, if d_m is differentiable at \mathbf{a} , then $\text{grad}_{\mathbf{a}} d_m = \mathbf{v}_m/d_m$. This property that is unique to the Euclidean norm is proven in detail in [25]. Therefore, following the chain rule of differentiation $\partial d_m(\mathbf{c}_l)/\partial c = \text{grad}_{\mathbf{a}} d_m \cdot \partial \mathbf{a}/\partial c$ [in our case, where the deformation approximated by the wavelet decomposition in (1)], it follows that for any wavelet coefficient $c = c_{jk}^{is}$

$$\frac{\partial d_m(\mathbf{c}_l)}{\partial c} = \frac{\partial d_m(\mathbf{c}_l)}{\partial c_{jk}^{is}} = \frac{v_m^i}{d_m} \Phi^s(2^{-j} \mathbf{x}_m - \mathbf{k}).$$

B. $L(\mathbf{c})$ —Elastic Energy

The second term $L(\mathbf{c})$ that is being minimized is the elastic energy, given by

$$L(\mathbf{c}) = \int \left[\mu \sum_{p=1}^2 \sum_{q=1}^2 \left(\frac{\partial u^p}{\partial x_q} \right)^2 + (\mu + \lambda) \left(\frac{\partial u^1}{\partial x_1} + \frac{\partial u^2}{\partial x_2} \right)^2 \right] d\mathbf{x} \quad (5)$$

where μ and λ are the Lamé's coefficients that reflect the elastic properties of the medium. Expanding the integral in (5) yields

$$L(\mathbf{c}) = \int \left[2 \left(\frac{\partial u^1}{\partial x_1} \right)^2 + \left(\frac{\partial u^1}{\partial x_2} \right)^2 + \left(\frac{\partial u^2}{\partial x_1} \right)^2 + 2 \left(\frac{\partial u^2}{\partial x_2} \right)^2 + 2 \frac{\partial u^1}{\partial x_1} \frac{\partial u^2}{\partial x_2} \right] d\mathbf{x} \quad (6)$$

where for simplicity we set $\mu = 1$ and $\lambda = 0$ (following the choice made by [14]). Substituting the signal as represented in (1) results in a linear combination of the integral

$$h_{pq}^{st}(j, l, \mathbf{k}, \mathbf{n}) = \int \frac{\partial \Phi^s(2^{-j} \mathbf{x} - \mathbf{k})}{\partial x_p} \frac{\partial \Phi^t(2^{-l} \mathbf{x} - \mathbf{n})}{\partial x_q} d\mathbf{x}$$

where $p, q = 1, 2$. (An analytic evaluation of this integral is presented in [26].) In order to simplify the expression for the elastic energy, we assume that the scaling and wavelet functions satisfy a principle we define and refer to here as *quasi-orthogonality of order three*. The quasi-orthogonality of order three property states that the scaling and wavelet functions are orthogonal to each other and orthogonal to each other's first and second derivatives. The consequence of satisfying this property of triple orthogonality is that the mix terms of $h_{pq}^{st}(j, l, \mathbf{k}, \mathbf{n})$ (terms with the basis functions from the different resolution levels ($j \neq l$) and different orientations ($s \neq t$) are canceled. In this study, merely orthogonal wavelets were used in which case the mix terms are negligible [26].

Let us continue and develop the expression in (6) for one signal component $w^i(j, s) = \sum_{\mathbf{k}=0}^{\mathbf{N}_j-1} c_{jk}^{is} \Phi^s(2^{-j} \mathbf{x} - \mathbf{k})$. In this case, (6) is a linear combination of the following terms:

$$\int \left[\frac{\partial w^i}{\partial x_p} \frac{\partial w^l}{\partial x_q} \right] d\mathbf{x}$$

$$= \sum_{\mathbf{n}} \sum_{\mathbf{k}} c_{jk}^{is} c_{jn}^{ls} \int \frac{\partial \Phi^s(2^{-j} \mathbf{x} - \mathbf{k})}{\partial x_p} \frac{\partial \Phi^s(2^{-j} \mathbf{x} - \mathbf{n})}{\partial x_q} d\mathbf{x}$$

$$= \sum_{\mathbf{n}} \sum_{\mathbf{k}} c_{jk}^{is} c_{jn}^{ls} h_{pq}^s(j, \mathbf{k}, \mathbf{n}) \equiv \mathbf{c}_j^{isT} \mathbf{Q}_{j pq}^s \mathbf{c}_j^{ls}. \quad (7)$$

Accordingly, the energy of the signal portion that corresponds to level j and orientation s is

$$L_j^s(\mathbf{c}_j^s) = \mathbf{c}_j^{1sT} (2\mathbf{Q}_{j11}^s + \mathbf{Q}_{j22}^s) \mathbf{c}_j^{1s} + \mathbf{c}_j^{2sT} (\mathbf{Q}_{j11}^s + 2\mathbf{Q}_{j22}^s) \mathbf{c}_j^{2s} + 2\mathbf{c}_j^{1sT} \mathbf{Q}_{j12}^s \mathbf{c}_j^{2s}. \quad (8)$$

The matrix form of (8) is

$$L_j^s(\mathbf{c}_j^s) = \begin{bmatrix} \mathbf{c}_j^{1sT} & \mathbf{c}_j^{2sT} \end{bmatrix} \cdot \begin{bmatrix} 2\mathbf{Q}_{j11}^s + \mathbf{Q}_{j22}^s & \mathbf{Q}_{j12}^s \\ \mathbf{Q}_{j12}^s & \mathbf{Q}_{j11}^s + 2\mathbf{Q}_{j22}^s \end{bmatrix} \cdot \begin{bmatrix} \mathbf{c}_j^{1s} \\ \mathbf{c}_j^{2s} \end{bmatrix}$$

$$\equiv \mathbf{c}_j^{sT} \mathbf{Q}_j^s \mathbf{c}_j^s. \quad (9)$$

Hence the expression for the whole elastic energy is

$$L(\mathbf{c}) = \mathbf{c}_J^{1T} \mathbf{Q}_J^1 \mathbf{c}_J^1 + \sum_{j=R}^J \sum_{s=2}^4 \mathbf{c}_j^{sT} \mathbf{Q}_j^s \mathbf{c}_j^s \equiv \mathbf{c}^T \mathbf{Q} \mathbf{c} \quad (10)$$

where \mathbf{Q} is a block diagonal matrix given as

$$\mathbf{Q} = \text{diag}(\mathbf{Q}_J^1, \mathbf{Q}_J^2, \mathbf{Q}_J^3, \mathbf{Q}_J^4, \mathbf{Q}_{J-1}^2, \mathbf{Q}_{J-1}^3, \mathbf{Q}_{J-1}^4, \dots, \mathbf{Q}_R^2, \mathbf{Q}_R^3, \mathbf{Q}_R^4).$$

Note, however, that the matrix \mathbf{Q} depends only on the chosen support \mathbf{N} and the scaling and wavelet basis functions Φ_j^s . \mathbf{Q} does not depend on the object of interest (more specifically, the object's deformation). Therefore, \mathbf{Q} can be computed once off-line and then used for the deformation estimation of any input object data. It can be shown that the matrix \mathbf{Q} is linearly proportional to the Wavelet–Galerkin discretization matrix of the homogenous static Navier PDE [26]. This implies that minimizing the elastic energy is equivalent to solving the Navier PDE.

Finally, the elastic energy in (10) is expanded using Taylor series, in the vicinity of \mathbf{c}_l , to yield

$$L(\mathbf{c}) \cong \mathbf{c}_l^T \mathbf{Q} \mathbf{c}_l + (\mathbf{c} - \mathbf{c}_l)^T 2\mathbf{Q} \mathbf{c}_l + (\mathbf{c} - \mathbf{c}_l)^T \mathbf{Q} (\mathbf{c} - \mathbf{c}_l)$$

$$= \mathbf{c}_l^T \mathbf{Q} \mathbf{c}_l + \Delta^T 2\mathbf{Q} \mathbf{c}_l + \Delta^T \mathbf{Q} \Delta. \quad (11)$$

C. Parameters Optimization

The expressions developed above for the sum of squared contour distances, $e(\mathbf{c})$, and for the elastic energy, $L(\mathbf{c})$, are combined to result in the functional $E(\mathbf{c})$, given by

$$E(\mathbf{c}) = e(\mathbf{c}) + \omega \cdot L(\mathbf{c})$$

$$\approx e(\mathbf{c}_l) + \mathbf{c}_l^T \mathbf{Q} \mathbf{c}_l + \Delta^T (\mathbf{b} + 2\omega \mathbf{Q} \mathbf{c}_l)$$

$$+ \Delta^T (\mathbf{A} + \omega \mathbf{Q}) \Delta. \quad (12)$$

In general, the objective is to find Δ , a step in the parameter space that is in the direction that minimizes $E(\mathbf{c})$. Following the M-L optimization method [27], this can be done by solving:

$$(\mathbf{b} + 2\omega\mathbf{Q}\mathbf{c}_l) + [(\mathbf{A} + \omega\mathbf{Q}) + \alpha\mathbf{I}]\Delta = 0 \quad (13)$$

where \mathbf{I} is the identity matrix and α is a positive scalar. The smaller α is, the closer the M-L is to the Newton optimization method; the larger α is, the closer the M-L is to the gradient (steepest-descent) optimization method.

The M-L optimization is done iteratively as follows.

- 1) Initialize $\alpha = 3$ and $\mathbf{c} = \mathbf{0}$ and compute $e_0 = e(\mathbf{c})$ for M points along the test contour.
- 2) Compute the vector \mathbf{b} and the matrix \mathbf{A} .
- 3) Solve $[(\mathbf{A} + \omega\mathbf{Q}) + \alpha\mathbf{I}]\Delta_1 = -(\mathbf{b} + 2\omega\mathbf{Q}\mathbf{c}_l)$ and $[(\mathbf{A} + \omega\mathbf{Q}) + \alpha/10\mathbf{I}]\Delta_2 = -(\mathbf{b} + 2\omega\mathbf{Q}\mathbf{c}_l)$.
- 4) Compute $e_1 = e(\mathbf{c} + \Delta_1)$ and $e_2 = e(\mathbf{c} + \Delta_2)$.
 - If $\|\Delta_1\| < \tau (=0.0001)$, set $\mathbf{c} = \mathbf{c} + \Delta_1$ and exit.
 - Else if $e_2 < e_1$, set $\alpha = \alpha/10$, $\mathbf{c} = \mathbf{c} + \Delta_2$, $e_0 = e_2$. Go to step 2).
 - Else if $e_2 \geq e_1$ and $e_1 < e_0$ set, $\mathbf{c} = \mathbf{c} + \Delta_1$, $e_0 = e_1$. Go to step 2).
 - Else set $\alpha = 10\alpha$, Solve $[(\mathbf{A} + \omega\mathbf{Q}) + \alpha\mathbf{I}]\Delta = -(\mathbf{b} + 2\omega\mathbf{Q}\mathbf{c}_l)$ and repeat until $e(\mathbf{c} + \Delta) < e_0$ or until a maximum iteration number (=10) has been reached. Set $e_0 = e(\mathbf{c} + \Delta)$, $\mathbf{c} = \mathbf{c} + \Delta$ and go to step 2).

Note that the second step (computation of the vector \mathbf{b} and the matrix \mathbf{A}) requires mapping M points \mathbf{x}_m along the test contour using the current registration parameters \mathbf{c} and computing the contour distance $d_m \cong d(T(\mathbf{x}_m, \mathbf{c}), S_{\text{ref}})$ for each point \mathbf{x}_m . This is done by searching through the set of points along the corresponding reference contour. This distance computation that needs to be done at each iteration and for all the M test points is computationally expensive especially in the 3-D case. However, using a distance map can reduce computation time significantly [25].

As mentioned before, our implementation of the optimization algorithm is a progressive one. We take advantage of the multiresolution representation of the deformation and recover the wavelet parameters that define it in a coarse-to-fine order. We first approximate the deformation with the wavelet decomposition, in (1), including only the lowest resolution level ($j = J$) and the first orientation ($s = 1$). At this stage, we find $\hat{\mathbf{c}}_j^1$ that minimizes $E(\mathbf{c}_j^1)$ following the M-L optimization method described above. Then we use $\hat{\mathbf{c}}_j^1$ to map the test contour onto a new position that is now closer to the reference contour. The residual deformation that still exists between the test contour and the reference contour is then recovered using the rest of the wavelet decomposition components that represent the deformation “details” at its different resolutions and different orientations. Thus, we proceed to find the parameters $\hat{\mathbf{c}}_j^2$ that minimizes $E(\mathbf{c}_j^2)$ and use now $\hat{\mathbf{c}}_j^1$ and $\hat{\mathbf{c}}_j^2$ to map the test contour toward the reference contour. In the same manner we solve for

the other two subbands, $s = 2$ and $s = 4$, at resolution level $j = J$. We continue down the wavelet pyramid to the next level of resolution $j = J - 1$, solving for the different subbands at this level $s = 2, 3, 4$. Hence, the computation of the wavelet coefficients is done progressively until the estimation of all of the coefficients is completed.

To improve parameters estimation, iteration takes place also across resolution levels. For example, in the case where levels 6 to 3 are used, M-L iterations are performed within each level and orientation stepping through levels of resolution in the following order: 6, 5, 6, 5, 4, 6, 5, 4, 3. In this procedure, starting from the lowest resolution level, for each additional refinement of the deformation estimation the algorithm steps back and updates the estimate of the lower resolution levels’ parameters at the presence of the others, already estimated, resolution levels’ parameters. This procedure is shorter than implementing a full iteration through the all resolution levels (in this case, levels 6, 5, 4, 3, 6, 5, 4, 3, 6, 5, 4, 3) and we empirically verified that its results show comparable estimation accuracy.

In the sequel, we refer to the algorithm in which all wavelet parameters are optimized at once as “Full Marquardt–Levenberg (FML)” and to the algorithm in which the wavelet parameters are optimized progressively as “Progressive Marquardt–Levenberg (PML).”

IV. ALGORITHM EVALUATION

The evaluation of the registration algorithm developed in this study was done by applying a known nonlinear transformation to two closed contours—an ellipse and the external contour of a rat brain section—referred to as the test objects. These test objects were centered at a 128×128 rectangular support for which the deformation $u(\mathbf{x})$ was defined. The nonlinear transformation that was applied to the test objects to create the reference objects was composed of affine and elastic transformations as follows:

$$T_a(\mathbf{x}) = \begin{bmatrix} 1.05 & -0.05 \\ 0.02 & 0.95 \end{bmatrix} \mathbf{x} + [5, 5]^T$$

and

$$T_e(\mathbf{x}) = \begin{bmatrix} \cosh(\alpha)(\cos\beta + \sin\beta) + \cosh(\beta)(\cos\alpha + \sin\alpha) - 2 \\ \sinh(\alpha)(\cos\beta - \sin\beta) - \sinh(\beta)(\cos\alpha - \sin\alpha) \end{bmatrix} + \mathbf{x} \quad (14)$$

where $\alpha = 0.2(x - \bar{x})$ and $\beta = 0.2(y - \bar{y})$. The elastic transformation, which is an analytic solution of the homogenous static Navier PDE, was scaled to result in an average and a maximum deformation along the objects’ external contour that is about 5% and 15% of object radius, respectively. Fig. 3 shows (a) the nonlinear deformation as applied to the rat section and (b) the deformation without the translational component. The above transformation were applied to points along the test contour \mathbf{x}_{test} to result in the reference contour $\mathbf{x}_{\text{ref}} = T(\mathbf{x}_{\text{test}})$. The number of points used was approximately the number of the registration parameters.

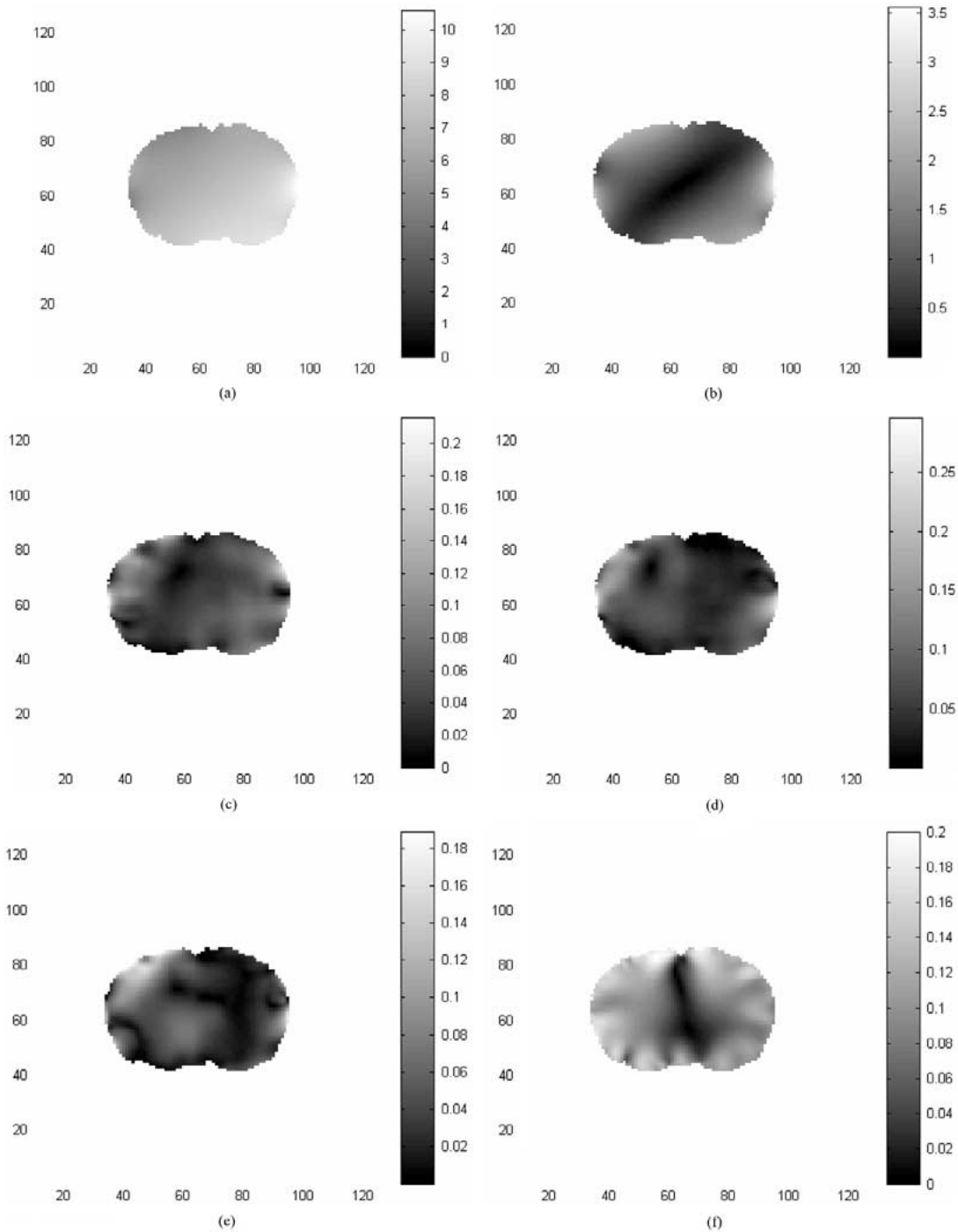


Fig. 3. (a) Deformation as applied to the rat section and (b) the deformation without the translational component. The resulted relative actual error, AE/ID , using the PML method with (c) Coif3, (d) Db5, and (e) Sym5 wavelets and (f) the TPS method.

The objective here was to estimate the applied deformation everywhere within the test object. We defined two types of errors: contour error (CE) and actual error (AE). The CE was defined by contour distance. As mentioned before, contour distance is the distance between a point on the test contour and the closest point to it on the corresponding reference contour (see Fig. 2), whereas AE is the distance between a test point and its corresponding reference point. We evaluated both types of error because in the experimental setting we do not know the actual point correspondence and, therefore, the AE is un-

known. Note that, by definition, the CE is always smaller than the AE.

Applying the FML and the PML optimization methods, including resolution levels 6 through 3, the test objects aligned onto their corresponding reference objects. The average initial deformation (ID), CE, and AE for the three orthogonal wavelets—Coif3, Db5, and Sym5—are shown in Tables I and II, respectively. We see that, in all cases, alignment error for the rat brain is smaller than that of the ellipse. It is possible that this occurs because a complex object's surface (in this case a

TABLE I
AVERAGE ID, CE, AND AE WHEN APPLYING NONLINEAR TRANSFORMATION
AND EMPLOYING THE FML METHOD (IN PIXELS)

Wavelet	Ellipse			Rat Brain Section		
	ID	CE	AE	ID	CE	AE
Coif3	7.10	0.35	0.62	7.07	0.25	0.40
Db5	7.10	0.38	0.63	7.07	0.25	0.42
Sym5	7.10	0.38	0.67	7.07	0.28	0.46

TABLE II
AVERAGE ID, CE, AND AE WHEN APPLYING NONLINEAR TRANSFORMATION
AND EMPLOYING THE PML METHOD (IN PIXELS)

Wavelet	Ellipse			Rat Brain Section		
	ID	CE	AE	ID	CE	AE
Coif3	7.10	0.35	0.59	7.07	0.27	0.35
Db5	7.10	0.38	0.59	7.07	0.31	0.43
Sym5	7.10	0.37	0.54	7.07	0.23	0.29

rat brain section) provides more information about the actual correspondence than is provided by the surface of a symmetric object (in this case an ellipse). In addition, we see that there was no significant difference in alignment accuracy when using different orthogonal wavelets. Tables I and II show that there was no significant difference in alignment accuracy between the FML and PML, though the running time of FML was ~ 20 min while this of the PML was ~ 10 min. Note that the PML method reduction of complexity is critically significant in the 3-D case where the number of parameters grows exponentially.

For example, Table II shows that, in the case where we used the Coif3 wavelet and the PML method to align the rat sections, the algorithm yielded for an average ID of 7.1 pixels an average AE of 0.35 pixels and an average CE of 0.27 pixels. Fig. 3 shows the relative actual error (ratio of AE and ID) everywhere within the rat section, using Coif3 [Fig. 3(c)], Db5 [Fig. 3(d)], and Sym5 [Fig. 3(e)] wavelets. It can be seen that in all of these cases the error is larger in the regions where there is a steeper change in deformation magnitude.

One of the advantageous characteristic of the wavelet-based alignment algorithm is its scalability. There is a tradeoff between the accuracy of the deformation approximation and the algorithm's complexity. This tradeoff can be controlled by the number of resolution levels included in the deformation estimation. For example, in the case where the Sym5 wavelet was used, Table III shows the improvement in alignment accuracy as the number of resolution levels grows. Also, Table III shows the number of registration parameters (wavelet coefficients) that were estimated. Note that, since only coefficients that correspond to basis functions that overlap the test object's boundary were included, the actual number of estimated registration parameters, especially at the higher resolution levels, may be lower than the maximum. For example, in the third level, 198 parameters were estimated out of the 256 parameters that exist in each orientation at this level (see the last row in Table III).

Graphs of the relative AE (ratio of AE and ID) and the relative CE (ratio of CE and ID) where the nonlinear transformation was applied to the rat section are shown in Fig. 4. The relative errors are shown for different resolution levels and as a function of section's concentric layers (external layer 1 through internals

TABLE III
AVERAGE ERROR AND ALGORITHM COMPLEXITY FOR THE REGISTRATION OF
RAT SECTIONS INCLUDING DIFFERENT RESOLUTION LEVELS

Res. (J - R)	CE	AE	Param. No.	Time (secs)
6 - 6	0.42	0.63	2x4x4	97
6 - 5	0.34	0.43	+2x3x16	207
6 - 4	0.27	0.34	+2x3x64	365
6 - 3	0.23	0.29	+2x3x198	585

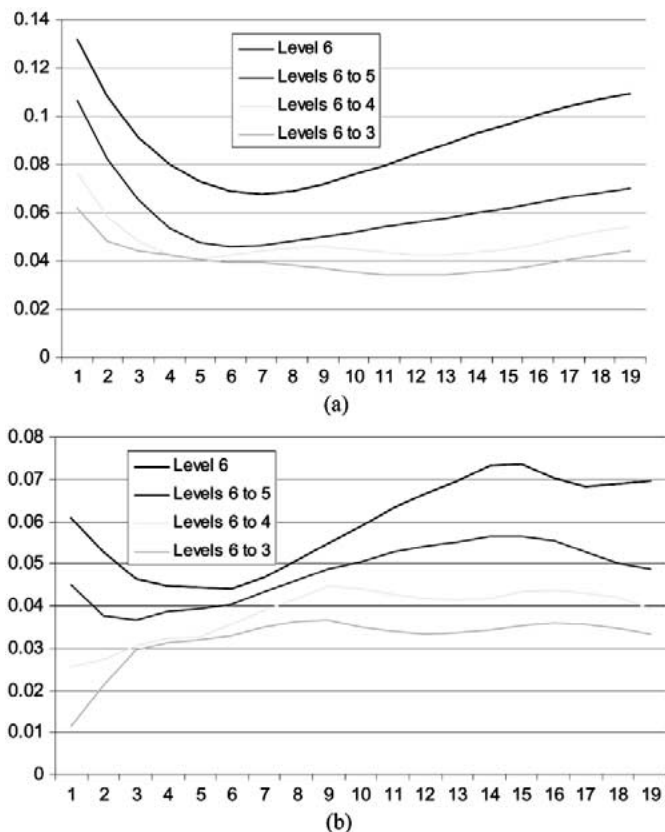


Fig. 4. (a) Relative actual error, AE/ID, and (b) relative contour error, CE/ID, in the case of the rat section alignment and when using Sym5 wavelet. The errors are shown for different resolution levels and as a function of concentric layers (external layer 1 through internals layers 2–20).

layers 2–20). The tradeoff between the approximation accuracy and the algorithm's complexity is apparent from Table III and Fig. 4: the more deformation estimation accuracy is desired, the more registration parameters and algorithm running time are required. The running times reported in this section are based on algorithm implementation using Matlab (version 6.1) on a Pentium IV computer (1.7 GHz, 1 GByte RAM).

Finally, the wavelet-based registration algorithm proposed in this study was compared with the Thin-Plate-Spline (TPS) algorithm as described by Gabrani and Tretiak [13]. As mentioned before, the TPS interpolates the elastic deformation between two objects using radial functions. Briefly, the TPS method provides a closed-form solution (and as such is relatively faster) that is composed of a linear system that satisfies a known deformation at a given number of corresponding points. In the TPS method, the number of registration parameters is directly proportional to the number of corresponding points used. Next,

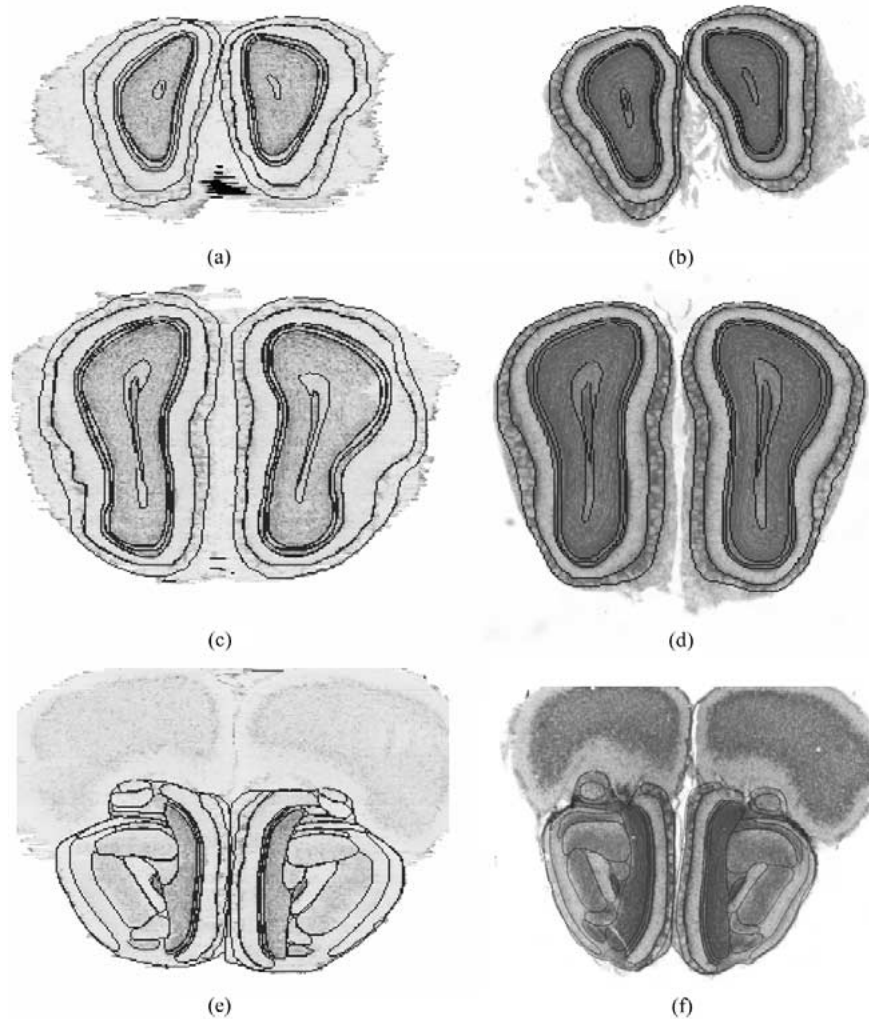


Fig. 5. Matching coronal sections from the atlas (left) and an experimental brain (right). The top pair (a) and (b) are located at a rostral level, the second pair (c) and (d) are located at an intermediate level, and the bottom pair (e) and (f) are located at a caudal level of the olfactory bulbs.

we aligned the rat sections to recover the nonlinear transformation with the TPS algorithm using different numbers of corresponding points.

Table IV shows the average ID, AE, and CE for different numbers of corresponding points. Apparently, increasing the number of corresponding points did not improve alignment accuracy. Fig. 3(f) shows the relative actual error everywhere within the rat section when using 96 corresponding points. The above results show that TPS yielded slightly lower CE values but larger AE values. However, note that TPS requires knowledge of a number of corresponding points that is not always available in an experimental setting. In Section V, we will test the TPS algorithm while using corresponding points that were estimated by the contour distance.

V. EXPERIMENTAL RESULTS

A. Data Acquisition

Eleven mouse brains (genetic strain C57BL/6J) were studied. One, the *reference* brain, was used to construct a 3-D brain volume atlas [28]. The other ten brains were the *test* brains. The test brains were embedded in celloidin and serially sectioned

TABLE IV
AVERAGE ID, CE, AND AE WHEN APPLYING NONLINEAR TRANSFORMATION AND EMPLOYING THE TPS METHOD

CPs	ID	CE	AE
32	7.07	0.19	0.54
96	7.07	0.18	0.54
192	7.07	0.22	0.61

coronally as described in [29]. Briefly, brains were dehydrated through a graded series of ethanol and ethanol/ether baths before being embedded in celloidin. The brains were cut coronally into 30- μm sections and every section saved. Floating sections were stained with cresyl violet. Each section was mounted on a glass slide and cover slipped with Permount.

The performance of the registration algorithm was evaluated in a 2-D setting. A matching reference section for each test section was defined visually using the MacOStat software package [30]. Three pairs of such corresponding 2-D coronal sections were defined from three different locations—rostral, intermediate and caudal levels of the olfactory bulbs, as is shown in Fig. 5. The high morphological variability between corresponding sections is clearly evident. Nineteen anatomical structures (see Table V for structures' Nomenclatures based on

TABLE V
LIST OF THE EXTERNAL/INTERNAL STRUCTURES IN THE MOUSE OLFACTORY

Structure	Description
GrO	granule layer, olfactory bulb
E/OV	ependyma & olfactory ventricle
aci	anterior commissure, intrabulbar
IPI	internal plexiform layer, olfactory bulb
Mi	mitral cell layer, olfactory bulb
EPI	external plexiform layer, olfactory bulb
Gl	glomerular layer, olfactory bulb
AOE	anterior olfactory nucleus, external
vn	vomer nasal nerve
EPIA	external plexiform layer accessory olfactory bulb
MiA	mitral cell layer, olfactory bulb
AOL	anterior olfactory nucleus, lateral
AOM	anterior olfactory nucleus, medial
AOD	anterior olfactory nucleus, dorsal
dlo	dorsolateral olfactory tract
GIA	glomerular layer, accessory olfactory bulb
lo	lateral olfactory tract
AOV	anterior olfactory nucleus, ventral
OB	olfactory bulb

the Franklin and Paxinos atlas [31]) were manually delineated on these sections, as shown in Fig. 5. The delineation of the test section was done on the images with a resolution of $4.3 \mu\text{m}/\text{pixel}$ while that of the reference brain was done with a resolution of $8.7 \mu\text{m}/\text{pixel}$.

B. 2-D Registration of Sections From the Olfactory Bulbs of the Mouse Brains

As mentioned above, three coronal sections were selected from each of ten experimental brains. Each section was aligned to its matching reference section. To do so a subset of the manually delineated contours—referred to as registration guiding (RG) structures—were used to guide the alignment process and the remaining ones—referred to as registration validating (RV) structures—were used for performance evaluation. We first aligned corresponding sections linearly and then recovered the nonlinear deformation everywhere within a support of 256×256 using the Coif3 wavelet and including resolution levels 7 through 3.

Two performance measures were computed for each structure and averaged across the ten brains: *error* (average residual contour distance between corresponding contours) and *overlap* (the area of the overlap of corresponding structures divided by the area of the reference structure). The error and overlap were computed for the data before the nonlinear alignment (after an affine transform was applied) and after the wavelet alignment.

Two cases were examined. In Case I, the external contour alone guided the registration, while in Case II the alignment was guided by the external contour as well as some internal ones.

Tables VI–VIII contain the results (the structures that guide the registration are denoted in bold). The three rows at the bottom of Tables VI–VIII show averages over all structures, weighted by structure area. We tabulate averages for RG structures, for RV structures, and for all structures (Total).

As can be seen from Tables VI–VIII the reduction of the error is substantial: on average (for all sections combined) from 3.4 to 1.5 for Case I and to 0.6 for Case II. The average increase in the overlap between corresponding structures is from 75% to 83% for Case I and to 91% for Case II. Fig. 6 shows sample images of alignment. The images in Fig. 6 show the reference sections and their structures' contours in dashed/blue lines. On the top of each section are drawn the contours of the corresponding mapped test section. Structures used to drive the alignment are shown in red and structures used for validation are shown in green. In the presence of high shape variability, the improvement of Case II over Case I is apparent.

The same experiments were conducted using the TPS registration method. Corresponding points were estimated as follows: 1) the test section was linearly aligned onto reference section; 2) points on the test contour were sampled at a distance of 10 pixels; and 3) then corresponding points to these were selected as the closest points from the corresponding reference contour. As can be seen from Tables VI–VIII, the performance of the wavelet—Case II method is significantly better than the TPS—Case II method. The average error that the wavelet—Case II method yielded was 0.6 compared with 1.5 yielded by the TPS—Case II method. The average overlap between corresponding structures was 91% in the wavelet—Case II and 84% in TPS—Case II. The results for TPS—Case I are not reported because they did not produce an improvement in alignment over the Affine alignment.

VI. CONCLUSION

A registration algorithm that compensates for nonlinear differences between two homologues elastic objects was presented. The application of wavelet multiresolution representation to the elastic deformation enabled complexity reduction of the optimization algorithm. The wavelet multiresolution representation allowed separate handling of the optimization procedure for parameters of different signal components. The method developed in this study, validated with synthetic data, showed promising results. The effectiveness of this registration algorithm as a means for anatomical localization of internal structures in the olfactory bulbs of mouse brains was also examined. Using a limited number of manually delineated structures from the olfactory bulbs, the wavelet-based alignment reduced the average error from 3.4 to 0.6 pixels and increased the average overlap from 75% to 91%.

These results compare favorably with other elastic methods. For example, the method by Gee *et al.* [32] used a probabilistic formulation of an image-based alignment problem using finite elements to represent the deformation field. The conditional probability between corresponding intensities was maximized, in addition to minimizing the distance between user-specified

TABLE VI
AVERAGE ERROR AND OVERLAP RATIO OF ROSTRAL SECTION ALIGNMENT

Structure	Affine		Wavelet - Case I		Wavelet - Case II		TPS - Case II	
	Error	Overlap	Error	Overlap	Error	Overlap	Error	Overlap
GrO	3.25	0.87	3.16	0.86	0.14	1.00	1.48	0.92
IPI	3.24	0.21	3.11	0.22	0.55	0.73	1.12	0.15
Mi	3.18	0.25	2.98	0.26	0.75	0.70	2.49	0.18
EPI	3.06	0.70	2.37	0.80	1.37	0.92	1.00	0.42
GI	3.16	0.66	0.77	0.83	1.04	0.72	1.71	0.45
OB	3.19	0.91	0.33	0.99	0.16	1.00	2.04	0.85
RG*	3.19	0.91	0.33	0.99	0.16	1.00	0.90	0.97
RV*	3.13	0.60	2.35	0.71	0.86	0.85	1.72	0.74
Total	3.16	0.75	1.36	0.84	0.52	0.92	1.32	0.85

* registration guiding structures, + validation guiding structures

TABLE VII
AVERAGE ERROR AND OVERLAP RATIO OF INTERMEDIATE SECTION ALIGNMENT

Structure	Affine		Wavelet - Case I		Wavelet - Case II		TPS - Case II	
	Error	Overlap	Error	Overlap	Error	Overlap	Error	Overlap
GrO	3.52	0.83	3.52	0.83	0.18	1.00	1.45	0.92
E/OV	2.84	0.26	3.18	0.26	1.67	0.50	2.46	0.33
aci	2.98	0.31	3.07	0.31	1.17	0.58	1.98	0.36
IPI	3.63	0.26	3.57	0.26	0.60	0.77	1.48	0.51
Mi	3.61	0.23	3.53	0.23	0.91	0.61	1.85	0.39
EPI	3.57	0.75	3.21	0.75	1.69	0.91	2.51	0.83
GI	3.48	0.71	1.68	0.71	1.27	0.74	1.94	0.66
OB	3.38	0.99	0.33	0.99	0.15	1.00	0.90	0.98
RG	3.40	0.92	0.33	0.99	0.15	1.00	0.91	0.98
RV	3.47	0.60	2.95	0.67	1.02	0.85	1.94	0.74
Total	3.43	0.76	1.67	0.83	0.59	0.92	1.43	0.86

TABLE VIII
AVERAGE ERROR AND OVERLAP RATIO OF CAUDAL SECTION ALIGNMENT

Structure	Affine		Wavelet - Case I		Wavelet - Case II		TPS - Case II	
	Error	Overlap	Error	Overlap	Error	Overlap	Error	Overlap
GrO	2.74	0.80	2.72	0.82	0.26	0.97	1.45	0.84
E/OV	2.12	0.40	2.15	0.43	1.71	0.50	1.96	0.46
aci	2.24	0.47	2.23	0.49	1.14	0.61	1.62	0.55
IPI	1.87	0.26	1.73	0.28	0.65	0.65	1.37	0.44
Mi	2.05	0.28	1.92	0.32	0.97	0.63	1.73	0.45
EPI	2.69	0.70	2.40	0.75	1.96	0.83	2.92	0.77
GI	2.38	0.49	2.12	0.58	2.24	0.56	2.28	0.41
AOE	4.46	0.40	4.77	0.34	2.59	0.75	3.59	0.55
vn	3.83	0.42	3.42	0.45	3.68	0.51	3.84	0.32
EPIA	3.60	0.30	3.76	0.25	2.64	0.35	4.96	0.19
MiA	4.84	0.33	4.91	0.30	3.30	0.52	5.83	0.31
AOL	3.46	0.75	3.65	0.76	0.20	0.97	1.74	0.82
AOM	3.74	0.44	3.71	0.43	2.84	0.57	3.42	0.41
AOD	3.67	0.73	4.20	0.67	0.27	0.96	1.97	0.74
dlo	4.35	0.18	4.55	0.20	2.72	0.40	4.35	0.20
GIA	3.81	0.50	3.46	0.50	3.27	0.62	4.23	0.37
lo	2.47	0.40	2.19	0.60	2.25	0.62	2.73	0.55
AOV	3.71	0.46	4.05	0.48	1.89	0.77	3.96	0.65
OB	4.06	0.90	0.36	0.99	0.22	0.99	1.02	0.97
RG	4.09	0.90	0.37	0.99	0.23	0.99	1.14	0.94
RV	2.91	0.58	2.82	0.62	2.07	0.66	2.87	0.53
Total	3.55	0.75	1.47	0.82	0.79	0.89	1.67	0.81

tie points and the elastic energy. In their experiments, using 2-D MRI images of the brain, the overlap of gray matter and ventricles (overlap defined by the area of intersection divided by the area of union) was measured and an increase from 75.5% to 79.6% was reported.

Another 2-D method was developed by Davatzikos *et al.* [33]. Here an elastic model to register 2-D MRI images onto a Talairach atlas was used. First, brain external contour and contours of ventricles were extracted using an active contour

algorithm and corresponding points were then located using a circular shift. Next, the slices were matched using nonlinear elastic transformation. This method was validated measuring the mean distance between 18 manually selected landmarks and yielded an average error reduction from 4.57 mm (3.3 mm std.) to 3 mm (2.8 mm std.). While the wavelet-based algorithm performed substantially better than both, it should be emphasized that comparison with these methods is difficult due to the different imaging modality.

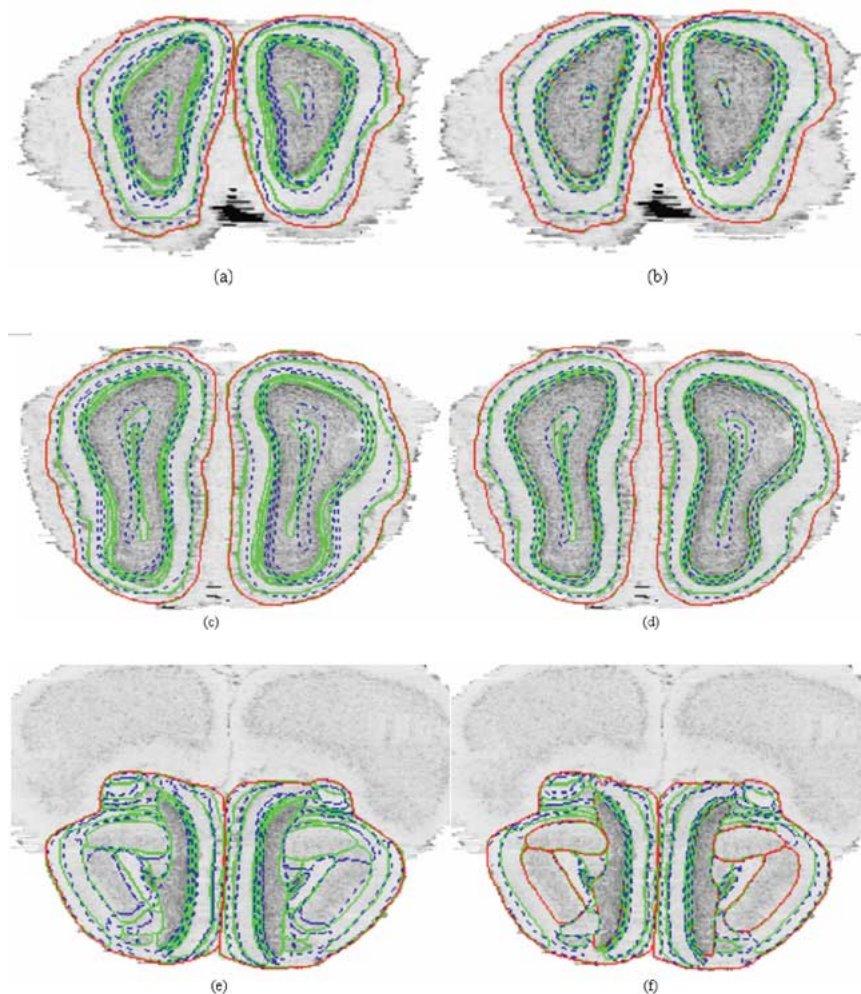


Fig. 6. Reference sections and their structures' contours are shown in dashed/blue lines. On the top of each section are drawn the contours of the corresponding mapped test section where structures used to drive the alignment are shown in red and structures used for validation are shown in green. Case I (left) and Case II (right) are shown for (a) and (b) caudal section, (c) and (d) intermediate section, and (e) and (f) rostral section.

The proposed wavelet-based algorithm's performance is promising in spite of having to overcome two main problems. The first problem being the large anatomical variability between corresponding structures in two different brains, as is evident from Fig. 6. The second problem was that the registration algorithm was applied to 2-D sections. Registration of two homologous sections (instead of registration of two brain volumes) requires the intermediate step of extracting two corresponding sections from the brain volumes. Since the elastic deformation that a test brain undergoes is in three dimensions, it is not plausible to have a test section that corresponds fully for an in-plane reference section. Therefore, modeling elastic deformation is likely to be more accurate when applied in the 3-D case. The generalization of the algorithm presented in this study into three dimensions is straightforward. In the future we plan to make this extension and evaluate the performance.

Another possible direction for future study is to investigate in greater detail the wavelet quasiorthogonality of order 3 property. In this study, we assumed that the compactly supported orthogonal wavelets approximately satisfied this triple orthogonality. However, one can design filter-banks that lead to quasiorthogonal wavelet of order 3 and study how these wavelets affect the registration accuracy.

REFERENCES

- [1] *Handbook of Medical Imaging*, I. N. Bankman, Ed., Academic, San Diego, CA, 2000.
- [2] A. W. Toga, *Brain Warping*. New York: Academic, 1999.
- [3] R. W. Thatcher, M. Hallett, T. Zeffiro, E. R. John, and M. Huerta, *Functional Neuroimaging—Technical Foundations*. San Diego, CA: Academic, 1994.
- [4] L. G. Brown, "A survey of image registration techniques," in *ACM Comput. Surveys*, vol. 24, 1992, pp. 325–376.
- [5] P. A. Van den Elsen, E. J. D. Pol, and M. A. Viergever, "Medical image matching—A review with classification," *IEEE Eng. Med. Biol. Mag.*, pp. 26–39, Mar. 1993.
- [6] J. West, J. M. Fitzpatrick, M. Y. Wang, B. M. Dawant, C. R. Maurer, R. M. Kessler, R. J. Maciunas, C. Barillot, D. Lemoine, A. Collignon, F. Maes, P. Suetens, D. Vandermeulen, P. A. Van Den Elsen, S. Napel, T. S. Sumanaweera, B. Harkness, P. F. Hemler, D. L. G. Hill, D. J. Hawkes, C. Studholme, J. B. Antoine-Maintz, M. A. Viergever, G. Malandain, X. Pennec, M. E. Noz, G. Q. Maguire, M. Pollack, C. A. Pelizzari, R. A. Robb, D. Hanson, and R. P. Woods, "Comparison and evaluation of retrospective intermodality brain image registration techniques," *J. Comput. Assisted Tomogr.*, vol. 21, pp. 554–566, 1997.
- [7] H. Lester and S. R. Arridge, "A survey of hierarchical nonlinear medical image registration," *Pattern Recognit.*, vol. 32, pp. 129–149, 1999.
- [8] J. Duchon, "Interpolation des fonctions de deux variables suivant le principe de la Flexion des plaques minces," in *RAIRO Analyse Numerique*, vol. 10, 1976, pp. 5–12.
- [9] J. Meinguet, "Multivariate interpolation at arbitrary points made simple," *Z. Angew. Math. Phys.*, vol. 30, pp. 292–304, 1979.
- [10] A. Goshtasby, "Registration of images with geometric distortions," *IEEE Trans. Geosci. Remote Sensing*, vol. 26, pp. 60–64, Jan. 1988.

- [11] F. L. Bookstein, "Principal warps: Thin-plate splines and the decomposition of deformations," *IEEE Trans. Pattern Anal. Machine Intell.*, vol. 11, pp. 567–585, June 1989.
- [12] M. Gabrani, *Multidimensional Spline Theory and Surface-Based Alignment of Brains, ECE*. Philadelphia, PA: Drexel Univ. Press, 1998.
- [13] M. Gabrani and O. J. Tretiak, "Surface-based matching using elastic transformations," *Pattern Recognit.*, vol. 32, pp. 87–97, 1999.
- [14] R. Bajcsy and S. Kovacic, "Multi-resolution elastic matching," *Comput. Vis. Graph. Image Processing*, vol. 46, pp. 1–21, 1989.
- [15] C. Broit, *Optimal Registration of Deformed Images*. Philadelphia, PA: Univ. Pennsylvania Press, 1981.
- [16] C. Davatzikos, "Nonlinear registration of brain images using deformable models," presented at the MMBIA'96, San Francisco, CA, June, 21–22 1996.
- [17] P. Thevenaz, U. E. Ruttimann, and M. Unser, "A pyramid approach to subpixel registration based on intensity," *IEEE Trans. Image Processing*, vol. 7, pp. 27–41, Jan. 1998.
- [18] Y. Amit, "A Nonlinear variational problem for image matching," in *SIAM J. Sci. Comput.*, vol. 15, 1994, pp. 207–224.
- [19] T. R. Downie, L. Shepstone, and B. W. Silverman. A wavelet based approach to deformable templates. presented at Image Fusion and Shape Variability Techniques
- [20] J. Deubler and J. C. Olivo, "A wavelet based multiresolution method to automatically register images," *J. Math. Imaging Vis.*, vol. 7, pp. 199–209, 1997.
- [21] M. Vetterli and J. Kovacevic, *Wavelets and Sub-Band Coding*. Englewood Cliffs, NJ: Prentice-Hall, 1995.
- [22] G. Strang and T. Nguyen, *Wavelets and Filter Banks*: Wellesley-Cambridge, 1997.
- [23] S. Mallat, *A Wavelet Tour of Signal Processing*. New York: Academic, 1999.
- [24] I. Daubechies, *Ten Lectures on Wavelets*. Philadelphia, PA: SIAM, 1997.
- [25] D. Kozinska, O. J. Tretiak, J. Nissanov, and C. Ozturk, "Multidimensional alignment using the euclidean distance transform," *Graph. Models Image Processing*, vol. 59, pp. 373–387, 1997.
- [26] S. Gefen, "Wavelet-based nonlinear multi-dimensional registration," Ph.D. dissertation, Drexel Univ., Philadelphia, PA, 2002.
- [27] D. W. Marquardt, "An algorithm for least-squares estimation of nonlinear parameters," *J. Soc. Indust. Appl. Math.*, vol. 11, pp. 431–441, 1963.
- [28] J. Nissanov, J. Eilbert, O. J. Tretiak, S. Gefen, S. Schremmer, C. Gustafson, and L. Bertrand, "3D atlases—Bridges between neurogenomics and neuroanatomy," in *Proc. IEEE Int. Symp. Biomedical Imaging*, Washington, DC, 2002, pp. 357–360.
- [29] G. D. Rosen, A. G. Williams, J. A. Capra, M. T. Connolly, B. Cruz, L. Lu, D. C. Airey, K. Kulkarni, and R. W. Williams. (2000) The mouse brain library @www.mbl.org.. presented at 14th Int. Mouse Genome Conf. [Online].
- [30] C. Gustafson, O. Tretiak, L. Bertrand, and J. Nissanov, "Design and implementation of software for assembly and browsing of 3D brain atlases," *Computer Methods and Programs in Biomedicine*, vol. 74, pp. 53–61, 2004.
- [31] K. B. J. Franklin and G. Paxinos, *The Mouse Brain in Stereotaxic Coordinates*. New York: Academic, 1997.
- [32] J. C. Gee, D. R. Haynor, M. Reivich, and R. Bajcsy, "Finite element approach to warping of brain images," *Proc. SPIE (Medical Imaging 1994: Image Processing)*, M. H. Loew, Ed., vol. 2167, pp. 327–337, May 1994.
- [33] C. Davatzikos, J. L. Prince, and R. N. Bryan, "Image registration based on boundary mapping," *IEEE Trans. Med. Imag.*, vol. 15, pp. 112–115, Feb. 1996.



Smadar Gefen (A'96–S'98–M'03) received the B.Sc. and M.Sc. degrees in electrical engineering from Tel Aviv University, Tel Aviv, Israel, in 1993 and the Ph.D. degree in electrical and computer engineering from Drexel University, Philadelphia, PA, in 2002.

Since 1993, she has been involved in research and development in the field of image processing. From 1995 to 1997, she was a Senior Engineer with Iterated Systems, Atlanta, GA, working on image and video compression, and from 1997 to 1998 she was an Associate Member of the Media Vision Group at Sarnoff Corporation, working on image registration. Currently she is a Postdoctoral Fellow with the Computer Vision Laboratory for Vertebrate Brain Mapping, Drexel University College of Medicine, Philadelphia. Her research interests include image classification, registration, and coding as well as wavelet theory and applications.

Since 1993, she has been involved in research and development in the field of image processing. From 1995 to 1997, she was a Senior Engineer with Iterated Systems, Atlanta, GA, working on image and video compression, and from 1997 to 1998 she was an Associate Member of the Media Vision Group at Sarnoff Corporation, working on image registration. Currently she is a Postdoctoral Fellow with the Computer Vision Laboratory for Vertebrate Brain Mapping, Drexel University College of Medicine, Philadelphia. Her research interests include image classification, registration, and coding as well as wavelet theory and applications.



Oleh Tretiak (S'56–M'63–SM'92) received the B.S. degree in electrical engineering from the Cooper Union, New York, NY, and the S.M. and Sc.D. degrees in electrical engineering from the Massachusetts Institute of Technology, Cambridge, MA.

He is the Robert C. Disque Professor of Electrical and Computer Engineering with Drexel University, Philadelphia, PA. His research deals with imaging and image processing, recently focusing on the theory and practice of neurocartography.



Louise Bertrand received the B.Sc. degree in biochemistry from Laval University, Quebec, QC, Canada in 1985.

From 1985 to 1996, she was a Research Assistant with the Neurobiology Research Center, Enfant-Jesus Hospital and Laval University, Quebec. From 1996 to 2000, she was a Research Specialist with the Department of Electrical and Computer Engineering at Drexel University, Philadelphia, PA. From 2000 to 2002, she was a Research Specialist with the Computer Vision Laboratory for Vertebrate

Brain Mapping, Drexel University College of Medicine. Since 2002, she has been a Lab Manager with the Computer Vision Laboratory for Vertebrate Brain Mapping and Co-instructor of Medical Neuroscience, Drexel University College of Medicine. Her current interests are quantitative neuroanatomy and development of computer vision tools for neuroanatomy.



Glenn D. Rosen received the A.B. degree in biology and psychology from Swarthmore College, Swarthmore, PA, in 1977 and the M.S. degree in biobehavioral sciences and the Ph.D. in developmental psychobiology from the University of Connecticut, Storrs, in 1980 and 1982, respectively.

For the past 21 years, he has been associated with the Dyslexia Research Laboratory at Beth Israel Deaconess Medical Center, Boston, MA, where he is currently its director. His academic appointment is at Harvard Medical School, where he is an Associate

Professor of Neurology (Neuroscience). His research interests include the anatomic substrates of developmental dyslexia and the genetic investigation of complex traits of the nervous system.



Jonathan Nissanov (M'95) received the B.A. degree in molecular biology and the Ph.D. degree in biology from the University of Colorado, Boulder, in 1979 and 1987, respectively.

He was a National Institutes of Health Postdoctoral Fellow from 1987 to 1989 at the Neurobiology Unit at the University of California, San Diego. After serving as a Research Associate (1989–1992) with the Department of Electrical and Computer Engineering, Drexel University, Philadelphia, PA, he joined the School of Biomedical Engineering, Science and Health Systems, Drexel University. Since 2000, he has been an Associate Professor with the Department of Neurobiology and Anatomy, Drexel University. His research interests are bioimaging, image analysis, and neuroinformatics.

He was a National Institutes of Health Postdoctoral Fellow from 1987 to 1989 at the Neurobiology Unit at the University of California, San Diego. After serving as a Research Associate (1989–1992) with the Department of Electrical and Computer Engineering, Drexel University, Philadelphia, PA, he joined the School of Biomedical Engineering, Science and Health Systems, Drexel University. Since 2000, he has been an Associate Professor with the Department of Neurobiology and Anatomy, Drexel University. His research interests are bioimaging, image analysis, and neuroinformatics.